

# Inelastic buckling behavior of steel members under reversed cyclic loading

Phill-Seung Lee<sup>a</sup>, Hyuk-Chun Noh<sup>b,\*</sup>

<sup>a</sup> Division of Ocean Systems Engineering, Korea Advanced Institute of Science and Technology, Daejeon, 305-701, Republic of Korea

<sup>b</sup> Department of Civil and Environmental Engineering, Sejong University, Seoul, 143-747, Republic of Korea

## ARTICLE INFO

### Article history:

Received 3 April 2009

Received in revised form

23 April 2010

Accepted 26 April 2010

Available online 26 May 2010

### Keywords:

Beam structures

Inelastic buckling

Finite elements

Nonlinear analysis

Hysteresis behavior

Steel structures

Cyclic loading

## ABSTRACT

The objective of this study is to simulate and investigate the inelastic buckling behavior of steel members under reversed cyclic loading. Cyclic inelastic buckling behavior is briefly discussed. Considering a large inelastic deformation, we propose a finite element discretization scheme for beam analysis that is simple and general. To verify the numerical model, the cyclic inelastic buckling behavior of beams is analyzed, and the solutions are compared with the experimental results. The proposed finite element procedure shows good predictive capability for simulating the inelastic buckling behavior of beam members under reversed cyclic loading. We perform various numerical experiments to investigate the reduction behavior of critical loads under cyclic load reversals depending on the slenderness ratio and initial imperfection. It is observed that the reduction is largest for intermediate beams with a slenderness ratio around 80.

Crown Copyright © 2010 Published by Elsevier Ltd. All rights reserved.

## 1. Introduction

Steel frame structures have been widely used in offshore platforms, buildings, lattice towers, bridges and various industrial structures. Such structures are frequently braced to resist lateral loading. The load-bearing capacity of the structures depends on the buckling characteristic of the bracing members. During a severe earthquake, the structures are subjected to reversed cyclic loading, and subsequent inelastic buckling of the bracing members is encountered.

The Earthquake Engineering Research Center (EERC) has conducted various experimental tests and analytical studies of the cyclic buckling behavior of steel braces [1,2]. In addition, numerical approaches have been tried to simulate the complex behavior [3–9].

To analyze the inelastic buckling of braced frame structures, both large deformation kinematics and inelastic material behavior must be considered. In practice, the finite element method has been used as the primary tool to analyze beam structures [10]. The behavior of beam members undergoing large inelastic deformations is complex and difficult to predict using beam finite elements. In fact, full three-dimensional nonlinear behavior can be predicted more accurately using shell or solid finite elements. However, for structures with a large number of beam

members, such as buildings and lattice structures, this approach is not practical because of the significant modeling effort and computational time required.

It is not difficult to develop numerical procedures for large elastic deformation analysis of general section beams, and numerous successful results have been obtained. However, to additionally consider inelasticity for various section shapes, more research is still required [10–12].

In this study, we use the isoparametric beam (Timoshenko beam) finite element to simulate the inelastic buckling behavior of steel members under reversed cyclic loading. The isoparametric approach has been widely used for general curved beam finite elements. Since this type of beam finite element is degenerated from three-dimensional (3D) solid elements and is based on continuum mechanics, the formulation is general and effective, in particular, for nonlinear analysis [10–12].

To correctly predict the hysteresis behavior of steel structures, it is crucial to use the proper material model [13]. In this study, we simulate the cyclic behavior of steel by sequentially changing the material properties of Anand's metal model [14–16]. We also present how the material model affects the numerical solutions of the cyclic buckling analysis.

Under cyclic load reversals, the load-bearing capacity of the beam member decreases as the number of load cycles increases. This phenomenon has been identified, but the reduction behavior of the critical loads, which depends on slenderness and imperfections, has not been well studied. In this study, we investigate the behavior using the proposed numerical procedure, and the results are discussed.

\* Corresponding author. Tel.: +82 2 3408 3292; fax: +82 2 3408 4332.

E-mail address: [cpebach@sejong.ac.kr](mailto:cpebach@sejong.ac.kr) (H.-C. Noh).

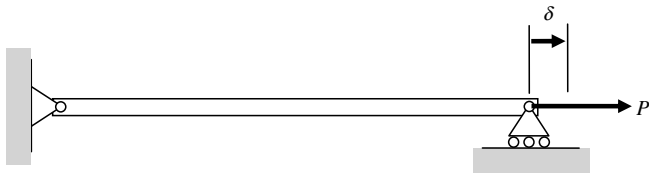


Fig. 1. A simply supported (pinned–pinned) beam problem.  $\delta$  is the prescribed displacement, and  $P$  is the (reaction) force.

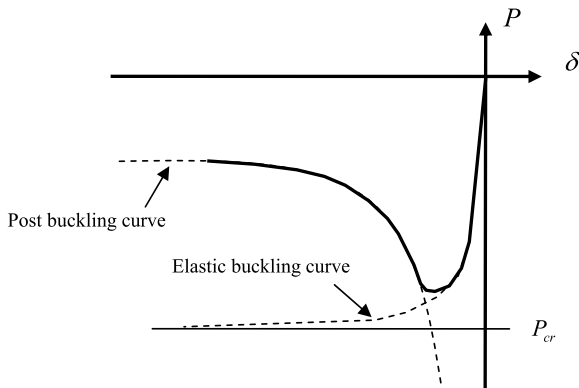


Fig. 2. Inelastic buckling behavior of beams.

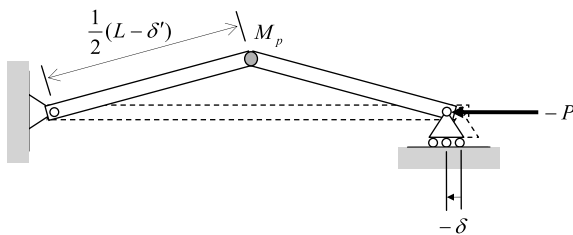


Fig. 3. Buckling of a simply supported beam of length  $L$  with a plastic hinge at mid-length.

In the following sections, we first discuss the inelastic buckling behavior of beam members under cyclic load reversals. Considering large deformation and inelasticity, we present a finite element discretization scheme to analyze the inelastic buckling of beam structures. Using the proposed numerical procedure, we perform inelastic buckling analyses under monotonic loading and simulate the inelastic buckling behavior of steel members

under reversed cyclic loading. The analysis results are verified by comparing them with those of experimental tests. We finally investigate the phenomenon of the critical load reduction of beam members through numerical experiments.

## 2. Inelastic buckling behavior

Fig. 1 displays a conceptual model of the experimental buckling test of beam members in [1]. Inelastic buckling behavior is well known under monotonic loads, and the typical load–displacement curve is shown in Fig. 2. The pre-buckling and post-buckling behavior of the simply supported beam of length  $L$  in Fig. 1 can be characterized by two curves that correspond to elastic buckling and post-buckling.

The elastic buckling capacity is given by

$$P = P_{cr}, \tag{1}$$

where  $P_{cr}$  denotes the critical load ( $P_{cr} = -\pi^2 \frac{EI}{L^2}$  for simply supported beams or pinned–pinned beams),  $E$  is Young's modulus and  $I$  is the minimum principal second moment of the area of the prismatic beam member. The typical elastic buckling curve of a beam with imperfections is shown in Fig. 2.

The post-buckling behavior can be approximated by

$$P = -\frac{2M_p}{\sqrt{(L - \delta')^2 - (L + \delta)^2}}, \tag{2}$$

where  $M_p$  is the plastic moment of the beam section (which depends on section shapes and material properties),  $\delta'$  is the shortening of the beam length due to axial compression and bowing,  $\delta$  is the prescribed displacement and  $P$  is the reaction force corresponding to  $\delta$ . Eq. (2) can be derived from the simple conceptual model in Fig. 3; see [11].

The inelastic buckling behavior of beam members under reversed cyclic loading has been experimentally studied, and the hysteresis behavior has been reported [1]. The beam member is initially compressed until the member buckles and is tensioned until it yields. We then compress the member to make it buckle again, and this loading sequence is repeated. Fig. 4 shows the load–displacement curve of the typical behavior, which can be obtained by displacement control.

The main feature of the response curve is that there exists a dramatic decrease in the buckling capacity of the beam member during load reversals. The reduction of the load-bearing capacity is a result of the residual displacement of the member (bowing) and the properties of the cyclic stress–strain relation of the steel during load cycles. The cyclic behavior has been explained in detail in [1–8].

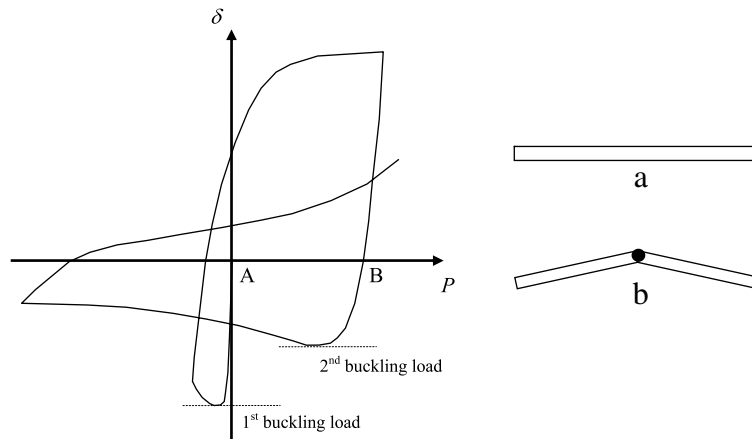


Fig. 4. Typical behavior of inelastic cyclic buckling (axial force–axial displacement curve): (a) initial geometry at point A; (b) residual deformed shape at point B.

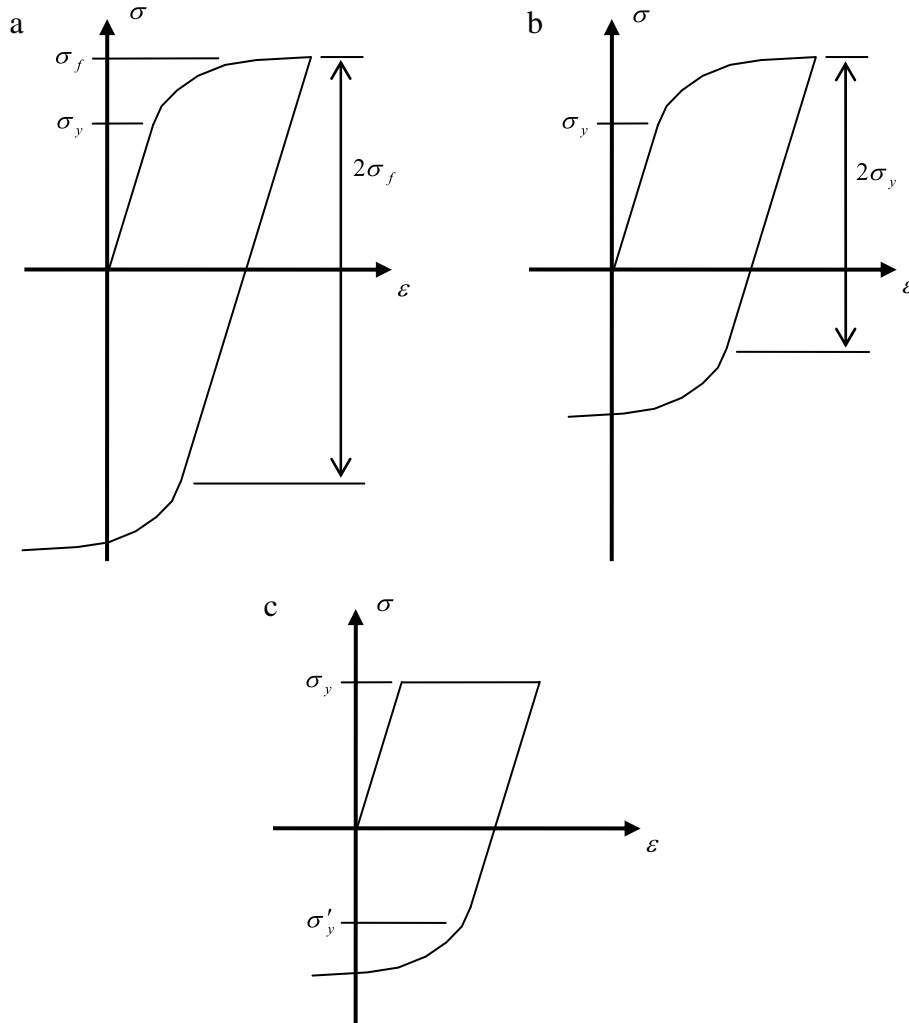


Fig. 5. Stress–strain relations: (a) isotropic hardening material; (b) kinematic hardening material; (c) change in yielding properties after the first yield.

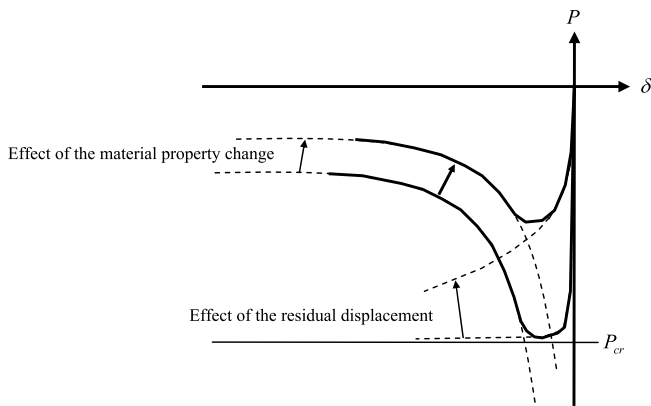


Fig. 6. Reduction in load-bearing capacity as a result of the residual displacement and material property changes.

Fig. 4(a) and (b) show the geometries of the beam when the axial force is zero before and after the first load cycle, respectively. The residual displacement after the first load cycle in Fig. 4(b) acts like the initial imperfection for buckling in the second load cycle.

Metals undergo strain hardening. Fig. 5 displays the stress–strain relations of an isotropic hardening material and a kinematic hardening material. The Bauschinger effect of steel can be modeled by kinematic hardening. However, since steel generally has both

hardening characteristics, the mixed hardening material model needs to be used for the material, in particular, when cyclic load reversals are considered.

For typical steel materials, the hardening rate is very small at the first yield; that is, rapid yielding occurs. However, for consecutive yields, the property changes into smooth hardening, as shown in Fig. 5(c). Also, after the first yielding, the yielding start point decreases from  $\sigma_y$  to  $\sigma'_y$  ( $\sigma'_y < \sigma_y$ ). This change in the stress–strain relation after the first yield affects the first reduction of the critical load.

Considering both the residual displacement of the member and the cyclic stress–strain relation properties, the reduction of buckling capacity under cyclic load reversals can be explained as shown in Fig. 6. The residual displacement describes the effect of increased imperfection, and the changes in the yield start point and the hardening property result in the decreased capacity of the plastic moment of the beam section, especially at the second buckling. Consequently, both effects reduce the load-bearing capacity; that is, the post-buckling curve of Eq. (2) moves up, as shown in Fig. 6.

### 3. Finite element discretization

To simulate the inelastic buckling behavior of steel beam members under reversed cyclic loading, both behaviors (the residual displacement and the cyclic stress–strain relation) can be predicted with reasonable accuracy in the finite element discretization.

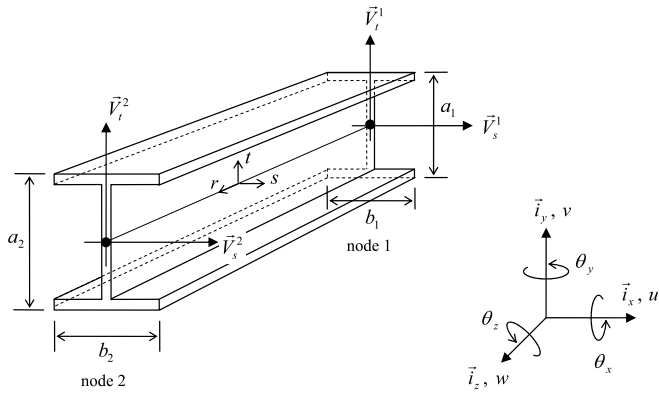


Fig. 7. Geometry of a two-node isoparametric beam element of a wide-flange section.

First, we consider large deformation kinematics to simulate the residual displacement. Of course, without large deformation kinematics, the buckling behavior cannot be predicted in the analysis model. Second, the inelastic material behavior, including the cyclic characteristics, is considered.

In beam analyses, there are two groups of schemes that consider inelastic behavior. Earlier, it was suggested that inelasticity at the resultant stress level of beam sections be addressed; in addition, the inelastic behavior has been frequently controlled at the stress–strain level at material points. In general, the former is more efficient when considering computational effort and the latter is more accurate, especially for a complex loading history, such as cyclic load reversals.

In previous research [11], the standard isoparametric beam (Timoshenko beam) element has been successfully modified to model angle section beams. The same approach can be used for other types of thin-walled section. We extend the approach for wide-flange sections and square-tube sections and implement the numerical procedure.

In this section, we briefly present the nonlinear formulation of a three-dimensional isoparametric beam finite element for elastoplastic large deformation analysis [10–12].

### 3.1. Thin-walled Timoshenko beam

In the Timoshenko beam theory, the basic assumption of beam kinematics is that plane cross sections originally normal to the central axis of the beam remain plane and undistorted under deformation but not necessarily perpendicular to the central axis of the deformed beam [10].

Considering the beam with a wide-flange section shown in Fig. 7, the geometry of the  $q$ -node beam finite element at time  $\tau^1$  is interpolated by

$$\begin{aligned} {}^\tau \vec{x}(r, s, t) = & \sum_{k=1}^q h_k(r) {}^\tau \vec{x}_k + \frac{t}{2} \sum_{k=1}^q a_k h_k(r) {}^\tau \vec{V}_t^k \\ & + \frac{s}{2} \sum_{k=1}^q b_k h_k(r) {}^\tau \vec{V}_s^k, \end{aligned} \quad (3)$$

where  $h_k(r)$  are the interpolation polynomials in the usual isoparametric procedures,  ${}^\tau \vec{x}_k$  are the Cartesian coordinates of node  $k$  at time  $\tau$ ,  $a_k$  and  $b_k$  are the cross-sectional dimensions at

node  $k$ , and the unit vectors  ${}^\tau \vec{V}_t^k$  and  ${}^\tau \vec{V}_s^k$  are the director vectors in directions  $t$  and  $s$  at node  $k$  and at time  $\tau$ . Note that  ${}^\tau \vec{V}_t^k$  and  ${}^\tau \vec{V}_s^k$  are normal to each other, as shown in Fig. 7. In this study, we use a two-node beam finite element ( $q = 2$ ).

Using the principle of virtual displacement, the linearized equilibrium equation in the total Lagrangian formulation is obtained for the beam finite element. The matrix form of the linearized equilibrium equation is

$${}^\tau_0 \mathbf{K} {}^\tau \mathbf{U} = {}^{\tau+\Delta\tau} \mathbf{R} - {}^\tau_0 \mathbf{F}, \quad (4)$$

where  ${}^\tau_0 \mathbf{K}$  is the tangent stiffness matrix at time  $\tau$ ,  ${}^\tau \mathbf{U}$  is the incremental nodal displacement vector,  ${}^{\tau+\Delta\tau} \mathbf{R}$  is the vector of externally applied nodal force at time  $\tau + \Delta\tau$ , and  ${}^\tau_0 \mathbf{F}$  is the vector of nodal forces equivalent to the element stresses at time  $\tau$ .

The isoparametric beam finite element was originally designed for solid rectangular sections. To use the element formulation for structural thin-walled sections (for example, angle, wide-flange and square-tube sections), a special integration scheme is required.

To calculate the tangent stiffness matrix and load vectors in Eq. (4), it is necessary to integrate them in the volume of the beam, which consists of  $n$  plates. For example, there are two plates for angle sections, three for wide-flange sections and four for square-tube sections; see Fig. 8.

The numerical integration for a generic matrix or vector function  $\mathbf{A}$  is

$$\int_V \mathbf{A} dV = \sum_n t_n \left[ \sum_{i,j} \det(\mathbf{J}_{ni}) \beta_i \beta_j \mathbf{A}(r_i, s_j, t_j) \right], \quad (5)$$

where  $t_n$  is the thickness of the plate  $n$ ,  $i$  denotes an integration point in the  $r$ -direction,  $\beta_i$  are the corresponding weight factors,  $j$  denotes the integration points in the  $s$ - $t$  plane and  $\beta_j$  are the corresponding weight factors in the plane. In Eq. (5),  $\det(\mathbf{J}_{ni})$  denotes the determinant of the Jacobian operator.

Fig. 8(a) shows the integration points for the elastic analysis of a wide-flange section beam finite element. For elastic analysis, two integration points per plate section are adequate (that is,  $2 \times 2$  Gauss integration points in each plate for a two-node beam element). However, more integration points in the plate sections are required for inelastic analysis, see Fig. 8(b) and (c), and the solution accuracy depends on the number of integration points used.

Note that, for the proposed beam finite element, thicker plates increase the discrepancy in sectional properties between the actual section and the section of the numerical model because of overlaps or gaps in the junctions of the plate sections, as shown in Fig. 8.

### 3.2. Material model

When a metal is first plastically deformed in tension and then compressed, the new yield stress in compression is smaller than the yield stress reached in tension. The same behavior is observed when the material is first compressed and then subjected to tension; that is, the subsequent yield stress in tension is smaller than the yield stress in compression [13].

This phenomenon is known as the Bauschinger effect, which can be explained by dislocation in the metal microstructure caused by plastic deformation. This effect is very important to include in the problem solution under reversed cyclic loading. In this study, a mixed hardening model that accounts for both the isotropic and kinematic hardenings is used to include the Bauschinger effect.

For finite element discretization, we use a one-dimensional rate-independent plasticity model with combined isotropic and kinematic hardening, given in [14–16], for the normal strain along the  $r$ -direction (the direction of beam length); see Fig. 7. Note that

<sup>1</sup> Here, we use the superscript  $\tau$  to denote time, but, in static analysis,  $\tau$  is a dummy variable that indicates load levels and incremental variables rather than actual time as in dynamic analysis [7].

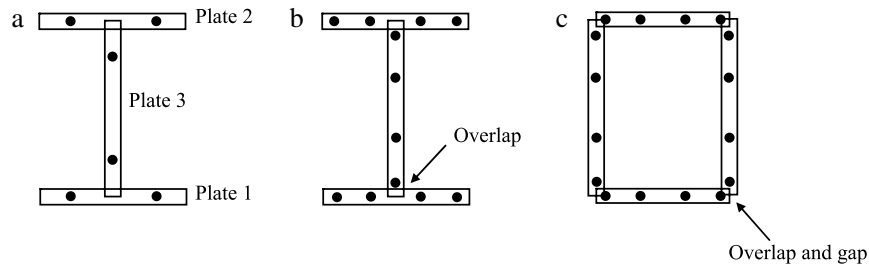


**Fig. 8.** Integration points of structural beam members: (a) two integrations per plate section in a wide-flange section; (b) four integrations per plate section in a wide-flange section; (c) four integrations per plate section in a square-tube section.

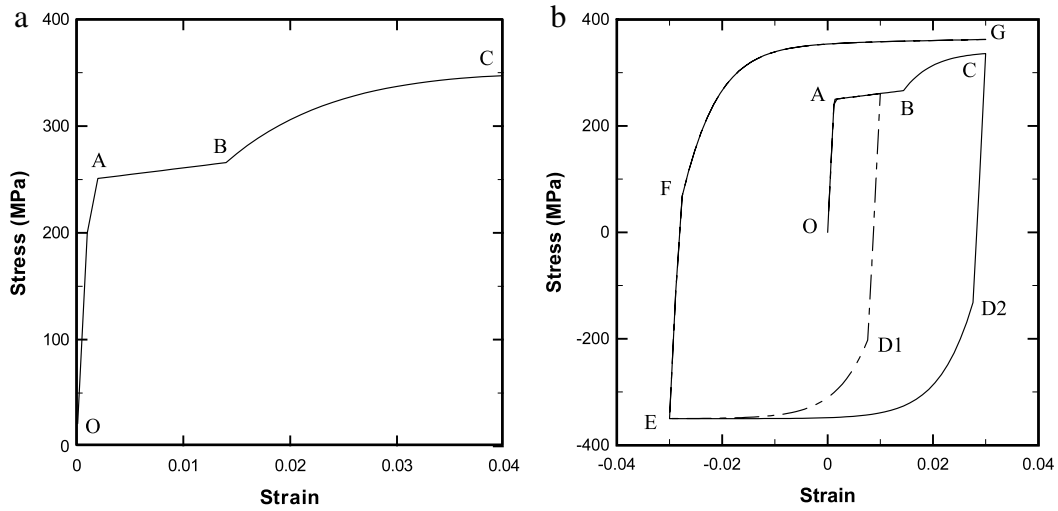


**Fig. 9.** Elastoplastic material model for steel: (a) monotonic behavior; (b) cyclic behavior.

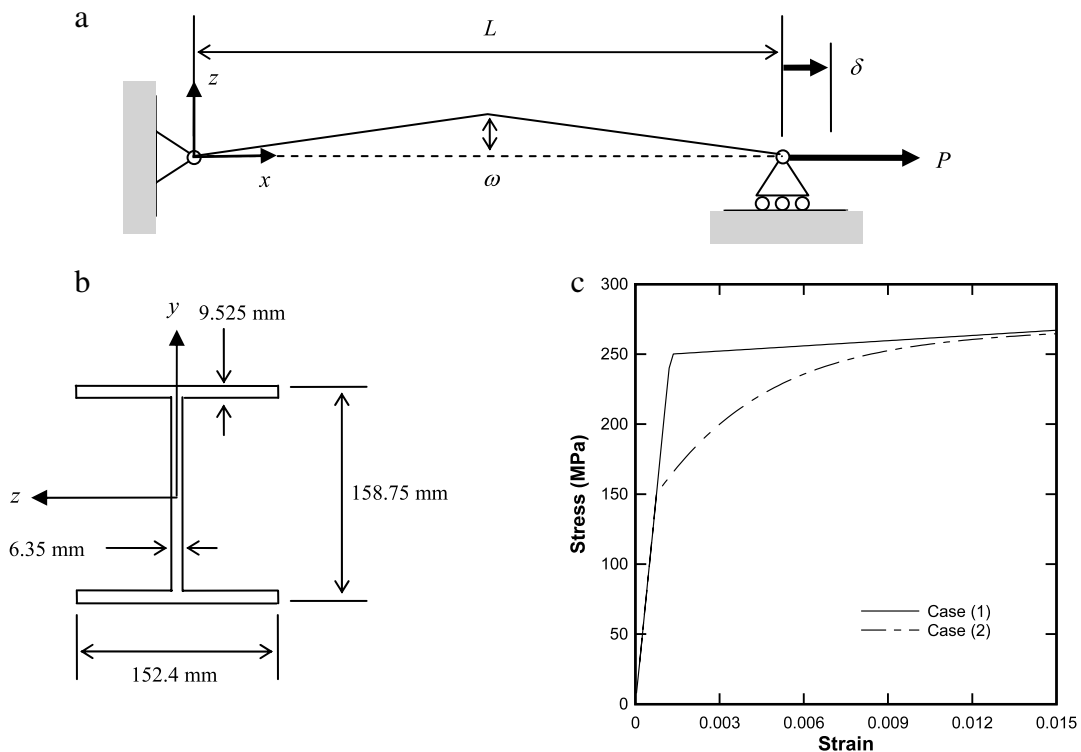


**Fig. 10.** Monotonic buckling analyses of a simply supported beam of a W6 × 20 section: (a) a simply supported beam with initial lateral displacement; (b) dimensions of a W6 × 20 section; (c) stress–strain curves of elastoplastic materials.

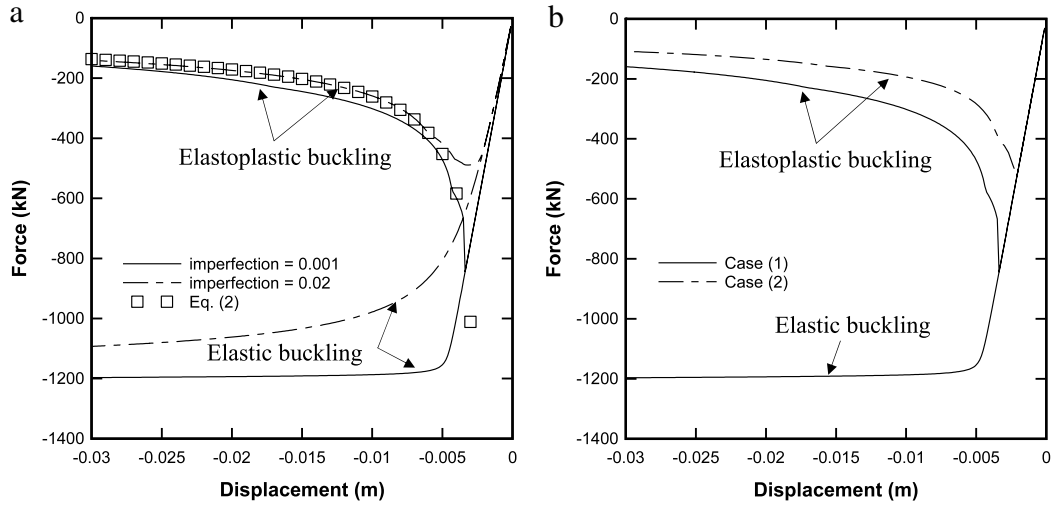


Fig. 11. Axial force-axial displacement curves: (a) effect of initial lateral displacements ( $\omega = 0.001$  m and  $\omega = 0.02$  m); (b) effect of stress-strain relations ( $\omega = 0.001$  m).

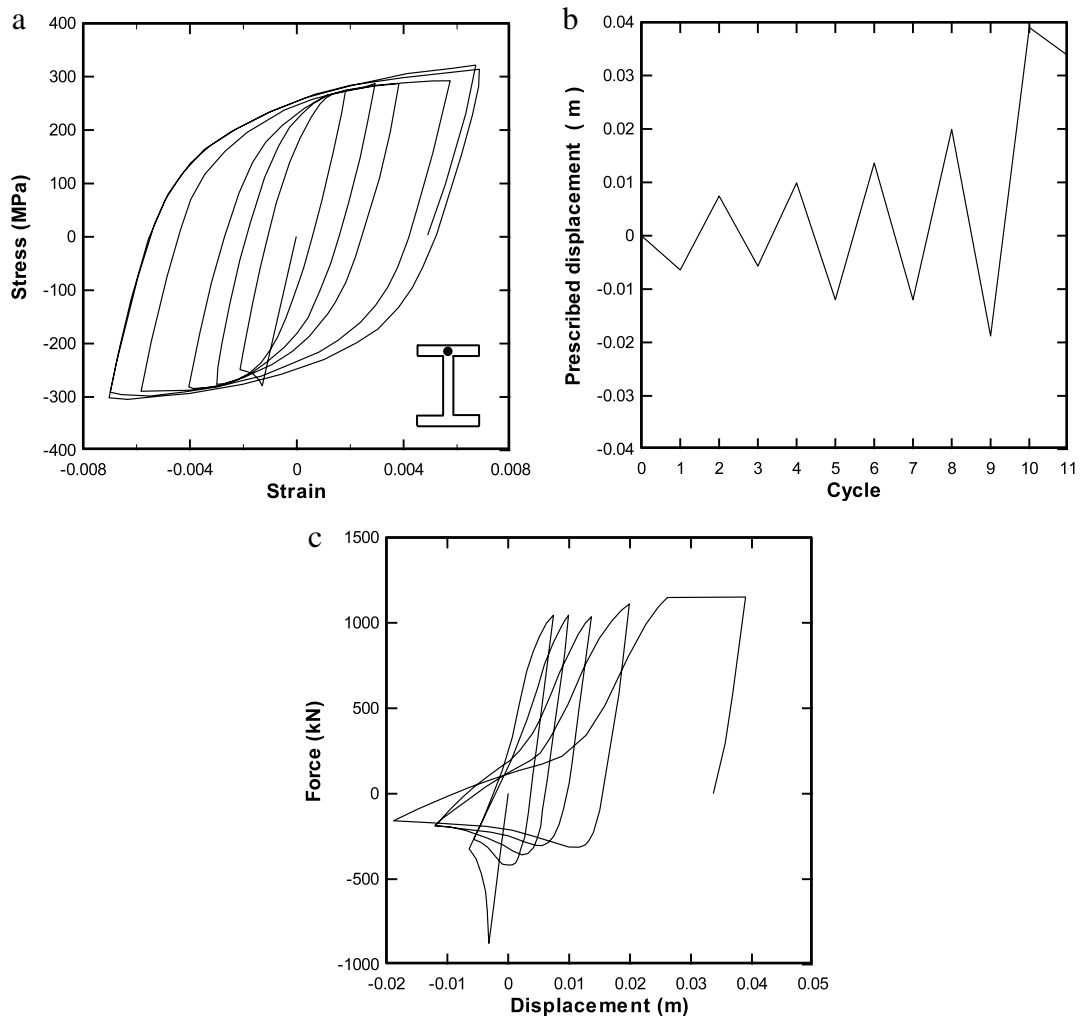


Fig. 12. Experimental results of W6 × 20: (a) stress-strain curve; (b) history of the prescribed displacement; (c) axial force-axial displacement curve.

it is more general to use an inelastic material model that can consider two additional transverse shear strains as well as the normal strain. However, a one-dimensional material model is sufficient for the analysis of this study because the normal strain is predominantly involved.

The normal strain  $\varepsilon$  is decomposed into two parts,

$$\varepsilon = \varepsilon_e + \varepsilon_p, \tag{6}$$

where  $\varepsilon_e$  and  $\varepsilon_p$  are the elastic and plastic parts of the normal strain along the beam length direction.

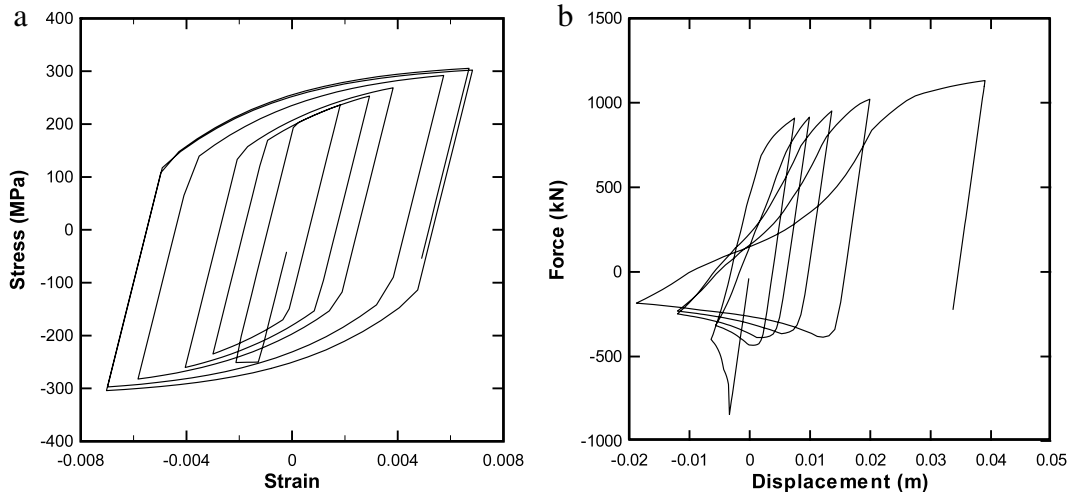


Fig. 13. Numerical results of W6 × 20: (a) stress–strain curve; (b) axial force–axial displacement curve.

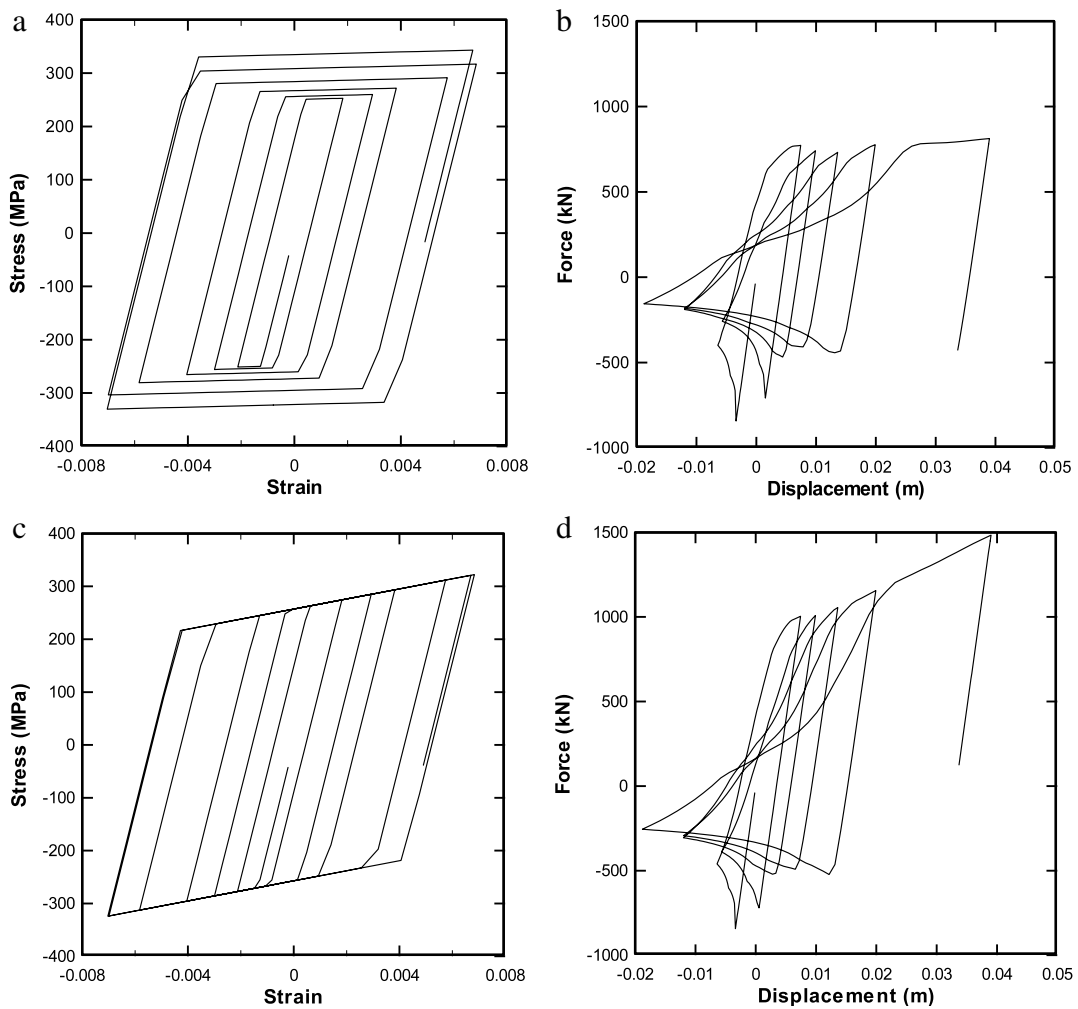


Fig. 14. Numerical results of W6 × 20: (a) stress–strain relationship for an isotropic hardening material; (b) axial force–axial displacement curve that corresponds to the isotropic hardening material; (c) stress–strain relationship for a kinematic hardening material; (d) axial force–axial displacement curve that corresponds to the kinematic hardening material.

The quadratic free energy is defined by

$$\psi = \frac{1}{2}E(\varepsilon_e)^2 + \frac{1}{2}C(A)^2, \tag{7}$$

in which  $E$  is Young’s modulus,  $A$  is an internal variable to describe the kinematic strain hardening and  $C$  is a constant that represents the stiffness that corresponds to  $A$ . We then obtain the equations

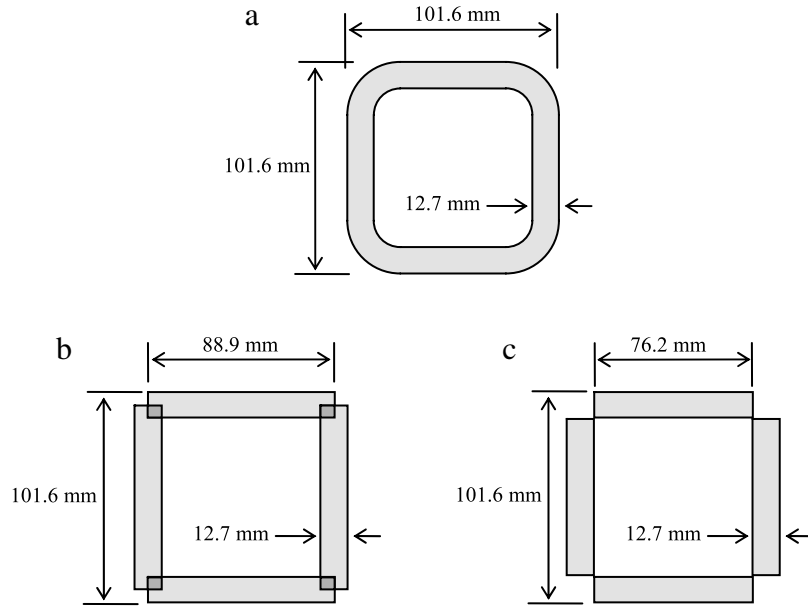


Fig. 15. Square-tube sections: (a) section of TS4 × 4 × 1/2; (b) numerical model of TS4 × 4 × 1/2; (c) effective section of TS4 × 4 × 1/2.

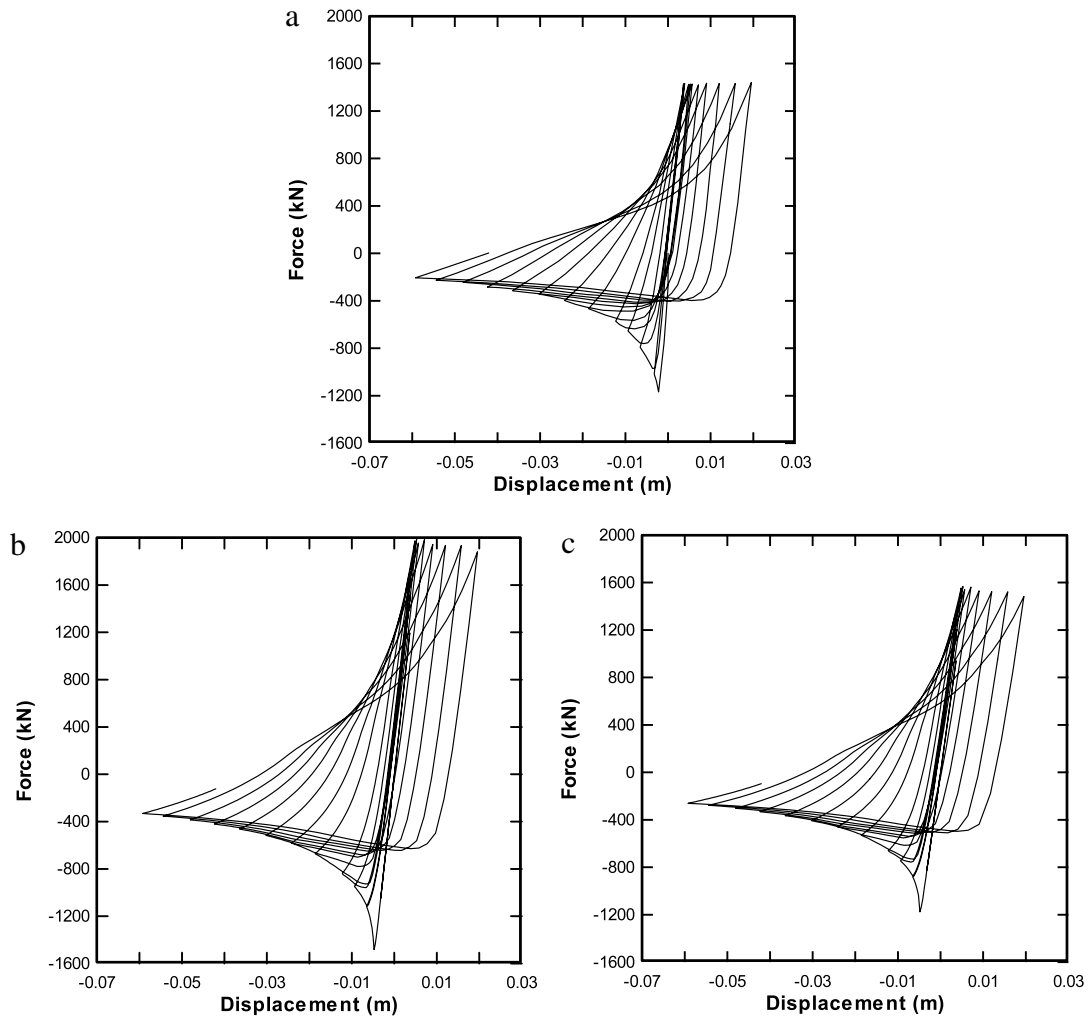


Fig. 16. Axial force–axial displacement curves of the square-tube section beams: (a) experimental result for the section in Fig. 15(a); (b) numerical result corresponding to the section in Fig. 15(b); (c) numerical result corresponding to the section in Fig. 15(c).

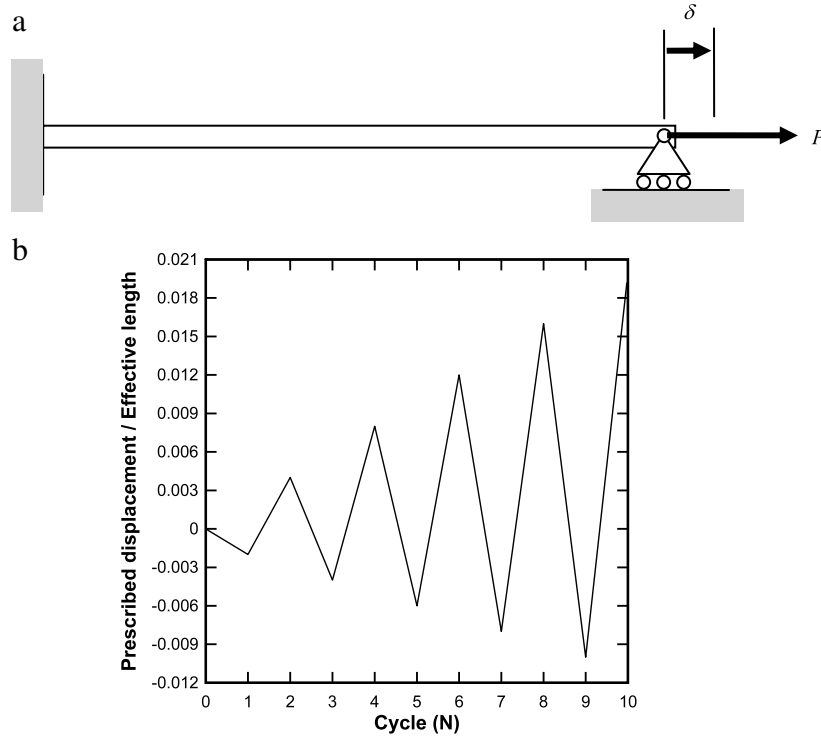


Fig. 17. (a) A beam with fixed–pinned conditions at the ends; (b) history of prescribed displacement in Eq. (16) that is normalized by the effective length  $kl$ .

for stress and back stress, respectively:

$$\sigma = \frac{\partial \psi}{\partial \varepsilon_e} = E(\varepsilon - \varepsilon_p), \quad \sigma_{\text{back}} = \frac{\partial \psi}{\partial A} = CA. \quad (8)$$

The plastic flow is given by

$$\dot{\varepsilon}_p = \lambda n^p, \quad n^p = \text{sign}(\sigma - \sigma_{\text{back}}) \quad \text{with } \lambda \geq 0, \quad (9)$$

where  $\lambda$  and  $n^p$  denote the flow rate and direction, respectively.

The stress state is restricted by a yield function

$$f = |\sigma - \sigma_{\text{back}}| - \sigma_y \leq 0, \quad \lambda f = 0, \quad (10)$$

where  $\sigma_y$  is the deformation resistance (yield stress), and the consistency condition that specifies the plastic flow rate is

$$\lambda \dot{f} = 0, \quad \text{if } f = 0. \quad (11)$$

The evolution equation for  $\sigma_y$  is

$$\dot{\sigma}_y = h\lambda \quad \text{with } h = h(\sigma_y), \quad \sigma_y(0) = \sigma_{y0}, \quad (12)$$

where  $h$  is a function that represents strain-hardening or strain-softening, and  $\sigma_{y0}$  is the initial value of the deformation resistance, that is, the initial yield stress. A particular form for the hardening function  $h$  that fits the data reasonably well for a metal is

$$h = h_0 \left(1 - \frac{\sigma_y}{\sigma_{ys}}\right)^a \quad \text{with } h_0 > 0, \sigma_y \leq \sigma_{ys}, \quad (13)$$

where  $h_0$ ,  $\sigma_{ys}$  and  $a$  are hardening parameters, and  $\sigma_{ys}$  denotes a saturation value of  $\sigma_y$  at which the hardening function becomes zero.

The evolution equation for the internal variable  $A$  is given by

$$\dot{A} = \dot{\varepsilon}_p - \gamma\lambda A \quad \text{with } A(0) = 0, \quad (14)$$

where  $\gamma$  is  $1/A_s$  and  $A_s$  represents a saturation value for  $|A|$ .

The presented material model is known to be simple and general. By changing the material properties ( $h_0$ ,  $\sigma_{y0}$ ,  $\sigma_{ys}$ ,  $a$ ,  $C$ ,  $\gamma$ ), the model can simulate various elastoplastic behaviors

of materials, including bilinear plasticity, power-law plasticity, isotropic hardening only and kinematic hardening only, as well as mixed hardening.

Fig. 9 displays typical stress–strain relationships of steel under monotonic and cyclic loadings. After the first elastic zone (O–A in Fig. 9), there exists a rapid yielding zone (A–B) at the initial yield, and then smooth hardening starts (B–C). During load reversals, the rapid yield zone disappears, and smooth hardening is repeated (D1–E, D2–E and F–G). A material model with one set of material properties cannot express the complex material behavior, that is, the first yielding and hardening (A–B–C) and the smooth hardening zones (D1–E, D2–E and F–G) together.

To simulate the typical stress–strain curve of steel using the proposed elastoplastic model, we successively use two or more different sets of material properties at the different zones. This is the key idea for material modeling to represent the complicated stress–strain behavior of steel under reversed cyclic loading. In this study, we use two different sets of material properties in the rapid yielding zone (A–B) and in the smooth hardening zones (D1–E, D2–E); see Fig. 9(b). Note that the zone B–C is not modeled because we assume that the material behaviors do not experience that particular zone. Also, we use the decreased initial yield stress  $\sigma'_y$  after the first yield, as mentioned in Section 2.

One-dimensional rate-independent plasticity with combined isotropic and kinematic hardening is implemented using the Euler-backward time-integration procedure.

#### 4. Numerical analysis

In this section, based on the finite element procedure presented, we analyze monotonic buckling problems and perform inelastic buckling analyses of beam members under reversed cyclic loading.

Cyclic axial loading experiments that simulate severe seismic condition for 24 structural steel struts have been reported [1]. We numerically simulate some of the experiments and discuss the results in detail.

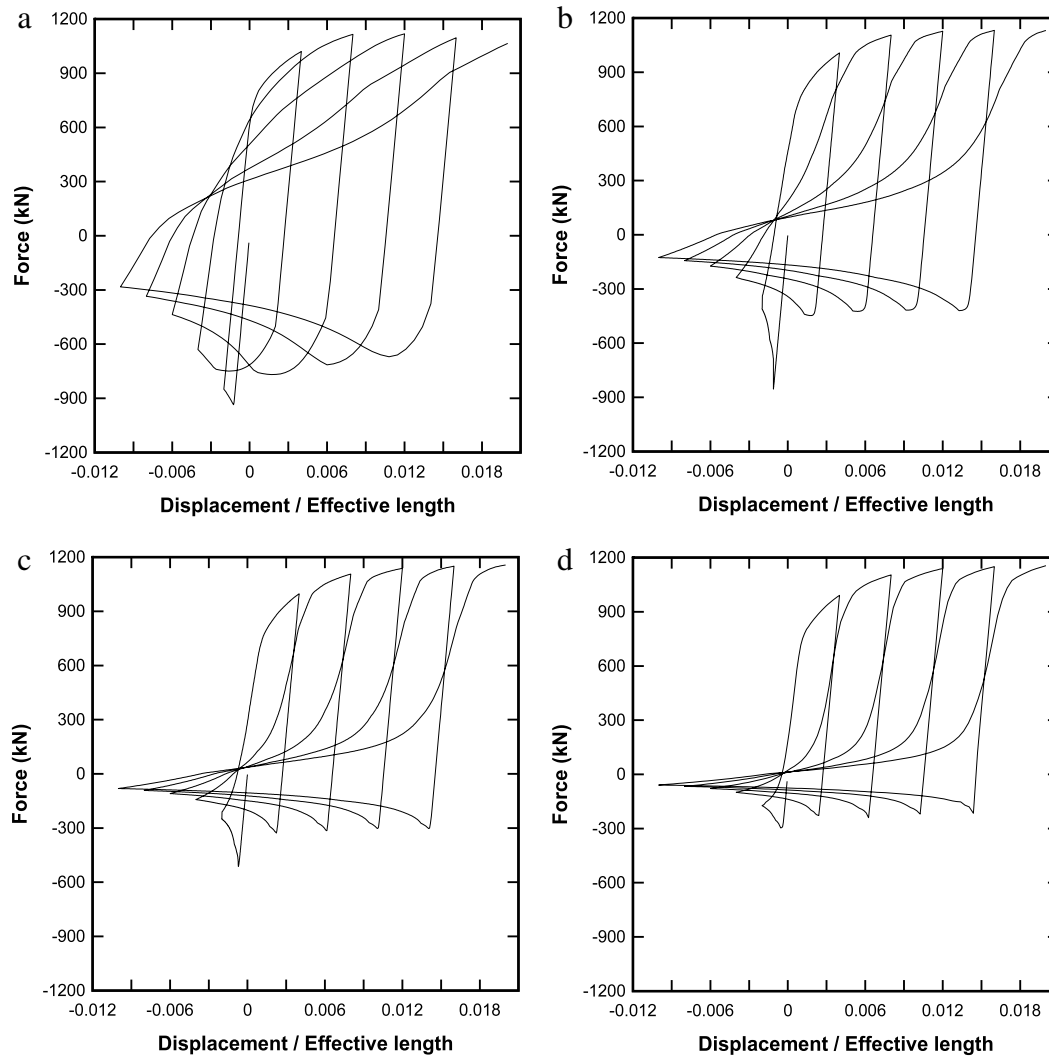


**Fig. 18.** Axial force–axial displacement curves of W6 × 20 depending on the slenderness ratio: (a) slenderness ratio = 40; (b) slenderness ratio = 80; (c) slenderness ratio = 120; (d) slenderness ratio = 160.

For all the numerical analyses, a uniform mesh of eight beam finite elements is used. In each element, four integration points in each plate section and one integration point along the beam length (in order to remove shear locking) are used. The solution accuracy, which depends on the number of elements used and the number of integration points per plate section, has been described for angle section beams in [11]. Note that, since similar results are obtained for thin-walled beams of other sections (wide-flange section and square-tube section), we do not present the results in this paper.

#### 4.1. Monotonic buckling analyses

Before analyzing the cyclic behaviors of steel members, we perform monotonic buckling analyses to investigate the effects of the residual displacement and the material property change in the stress–strain relation after the first yielding as discussed in Section 2. As shown in Fig. 10(a), a simply supported beam is subjected to the prescribed axial displacement  $\delta$  at the right end. The beam structure has an initial lateral displacement  $\omega$  at mid-length. The dimensions of the wide-flange section (W6 × 20) are shown in Fig. 10(b) and the beam length is 3.07 m. The Young's modulus of the material is  $E = 2 \times 10^{11}$  N/m<sup>2</sup>. Buckling occurs about the  $y$ -axis of the beam section in Fig. 10(b) because the second moment of the area about the axis is minimal.

As mentioned before, there are differences in sectional properties between the actual W6 × 20 section and the section of our numerical model because the fillet areas of the W6 × 20 section are not considered in the numerical model in addition to the sectional discrepancy mentioned in Section 3.1. The sectional area and the second moment of the area of the beam model are 0.7% bigger and 0.2% smaller than those of the actual wide-flange section (W6 × 20) used for the experimental test, respectively. In general, as the thicknesses of the flanges and web decrease, the differences become smaller. Note that the area and second moment of the area significantly affect the yield capacity in tension and the buckling capacity, respectively.

To investigate the effect of residual displacement, we perform buckling analyses by giving initial imperfections (initial lateral displacements). Considering two different initial lateral displacements ( $\omega = 0.001$  m and  $\omega = 0.02$  m), elastic and elastoplastic analyses are performed. For the analyses, elastoplastic material properties are used:

$$\begin{aligned} \text{(Case 1)} \quad & E = 2 \times 10^{11} \text{ N/m}^2, \quad \nu = 0.3, \\ & h_0 = 1.25 \times 10^9 \text{ N/m}^2, \quad \sigma_{y0} = 2.5 \times 10^8 \text{ N/m}^2, \\ & \sigma_{ys} = 2.5 \times 10^8 \text{ N/m}^2, \\ & a = 0, \quad C = 0, \quad \gamma = 0; \end{aligned}$$

the resulting bilinear stress–strain relation is displayed by the solid line in Fig. 10(c).

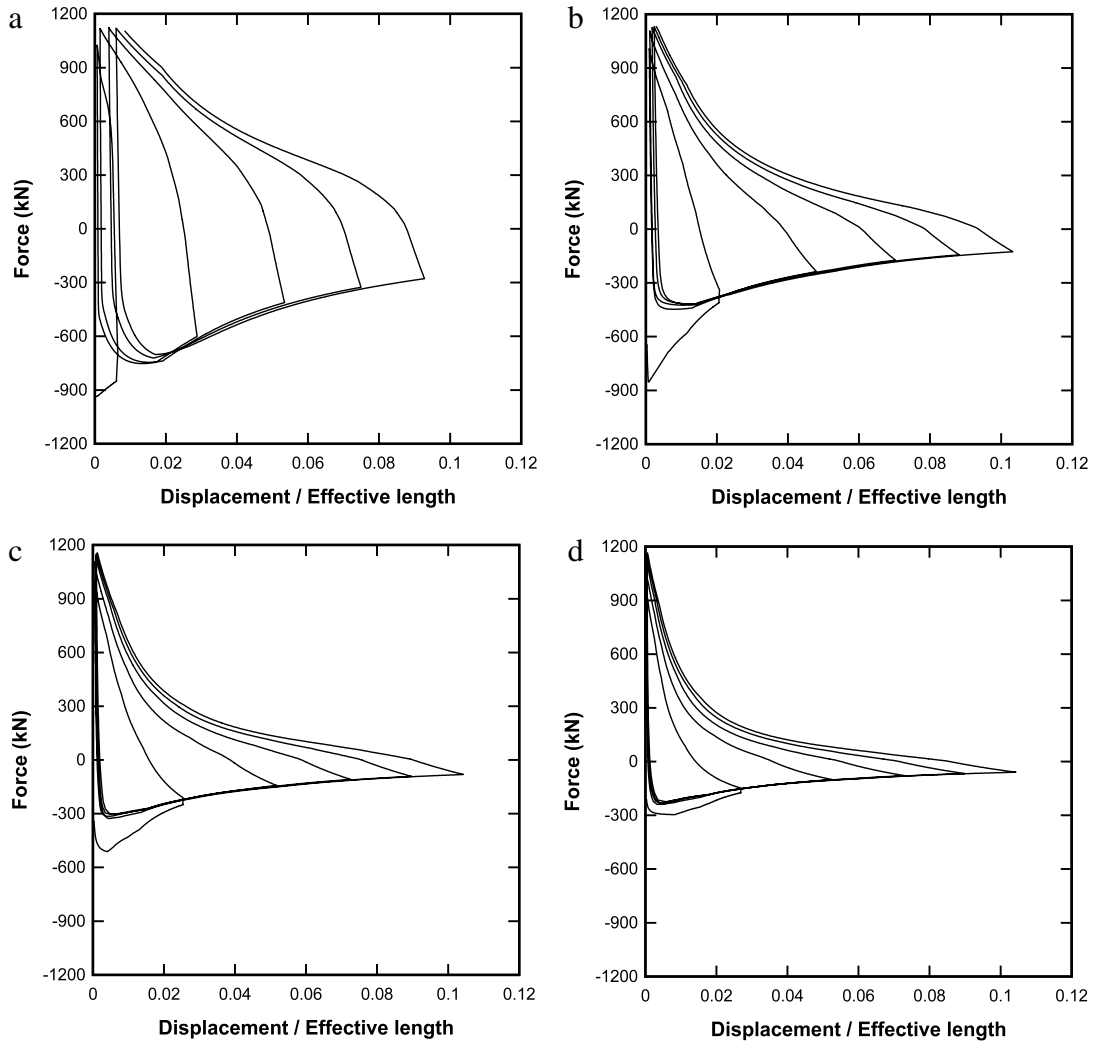


Fig. 19. Axial force–lateral displacement curves of W6 × 20 depending on the slenderness ratio: (a) slenderness ratio = 40; (b) slenderness ratio = 80; (c) slenderness ratio = 120; (d) slenderness ratio = 160.

Fig. 11(a) shows the numerical results of the relationships between the prescribed displacement and the reaction at the right end of the beam. Of course, the figure illustrates that a larger initial lateral displacement induces a smaller critical buckling load, and the post-buckling curves follow Eq. (2). We also note that the smaller imperfection gives the sharper peak at the point corresponding to the buckling load.

Another buckling analysis is performed to investigate the change in the load–displacement curve as a result of different material properties, in particular, the change in the stress–strain relation after the first yielding. We use the initial imperfection,  $\omega = 0.001$  m. We consider another material with different properties, as shown in Fig. 10(c).

$$\begin{aligned}
 \text{(Case 2)} \quad E &= 2 \times 10^{11} \text{ N/m}^2, & v &= 0.3, \\
 h_0 &= 1.25 \times 10^9 \text{ N/m}^2, & \sigma_{y0} &= 1.5 \times 10^8 \text{ N/m}^2, \\
 \sigma_{ys} &= 2.5 \times 10^8 \text{ N/m}^2, \\
 a &= 1.0, & C &= 3.3 \times 10^{10} \text{ N/m}^2, & \gamma &= 300.
 \end{aligned}$$

Note that cases 1 and 2 correspond to the material properties at the first yield and the second yield, respectively. Case 2 has smaller  $\sigma_{y0}$  and smoother hardening property than case 1.

Fig. 11(b) shows that the material properties of case 2 lead to a smaller critical load because the post-buckling curve shifts up, as mentioned in Section 2.

#### 4.2. Cyclic buckling analysis of a wide-flange section beam

As mentioned, experimental tests on the inelastic buckling of various beam members under cyclic load reversals have been reported [1]. We numerically simulate one of the tests and compare the results.

A beam member of wide-flange section (W6 × 20, Fig. 10(b)) is pinned at both ends, as shown in Figs. 1 and 10(a). The structure, of length 3.07 m, is subjected to the prescribed axial displacement  $\delta$  at the right end. The material of the beam is ASTM-A36 steel. Buckling occurs about the y-axis of the beam section; see Fig. 10(b).

Since information on imperfections has not been reported in [1], we use a very small initial lateral displacement  $\omega = 0.001$  m, which can produce the converged first buckling load. Note that, as the amount of the initial imperfection decreases, the buckling load increases and converges into a finite value.

For the wide-flange section beam, a coupon test was performed for a specimen at the center of the top flange, and the results are displayed in Fig. 12(a). Fig. 12(b) and (c) show the history of prescribed displacement and the axial force–axial displacement curve, respectively. These curves are digitized from the experimental results given elsewhere [1].

To simulate the cyclic behavior, we first try to obtain a stress–strain curve that is similar to the coupon test result. Fig. 13(a) presents the cyclic stress–strain relationship considering

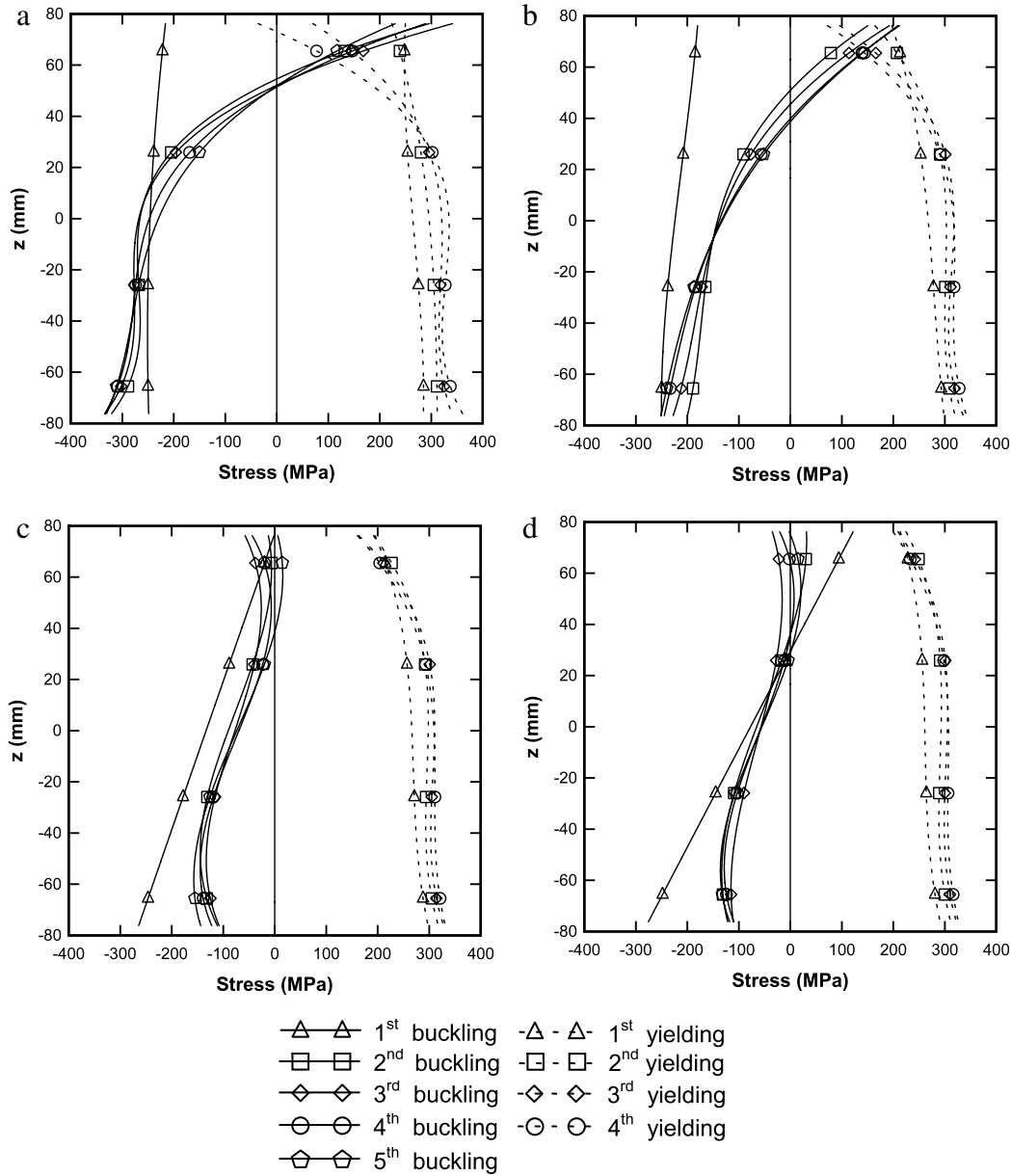


**Fig. 20.** Stress distributions along flange at mid-length that depend on the slenderness ratio (the pinned–pinned W6 × 20 beam problem): (a) slenderness ratio = 40; (b) slenderness ratio = 80; (c) slenderness ratio = 120; (d) slenderness ratio = 160.

the mixed hardening discussed in the previous section. The strain history used is the same as in the coupon test. To model the flat zone after the first yield point and the smooth strain hardening zones during load cycles, we use two different sets of material properties.

(1) For the rapid (initial) yield zone in the first cycle:

$$\begin{aligned}
 E &= 2 \times 10^{11} \text{ N/m}^2, & \nu &= 0.3, \\
 h_0 &= 1.25 \times 10^9 \text{ N/m}^2, & \sigma_{y0} &= 2.5 \times 10^8 \text{ N/m}^2, \\
 \sigma_{ys} &= 2.5 \times 10^8 \text{ N/m}^2, \\
 a &= 0, & C &= 0, & \gamma &= 0.
 \end{aligned}$$

(2) For the smooth hardening zones:

$$\begin{aligned}
 E &= 2 \times 10^{11} \text{ N/m}^2, & \nu &= 0.3, \\
 h_0 &= 1.25 \times 10^9 \text{ N/m}^2, & \sigma_{y0} &= 2.5 \times 10^8 \text{ N/m}^2, \\
 \sigma_{ys} &= 2.5 \times 10^8 \text{ N/m}^2, \\
 a &= 1.0, & C &= 3.0 \times 10^{10} \text{ N/m}^2, & \gamma &= 300.
 \end{aligned}$$

Note that, in both material properties used, only  $a$ ,  $C$  and  $\gamma$  are different. The decreased yield stress after the first yield  $\sigma'_y = 2.0 \times 10^8 \text{ N/m}^2$  is used.

Fig. 13(b) presents the numerical result of the axial force–axial displacement relation. It is observed that the numerical result predicts the experimental response well. [1] reports that the inelastic material property was not homogeneous at the beam section and the cyclic coupon test was performed at only one material point. If we use better material properties that can effectively represent the material behavior of the section, better numerical prediction would be obtained. It is reported that local buckling near the beam center was observed in the experiment [1] and, of course, this had some effect on the experimental results. However, the beam model used in this study cannot capture the local buckling behavior because of the limitations of beam theory.

To show the dependence of the hysteresis response on material behaviors, we consider two additional cases.

(Case 1) Isotropic hardening material as shown in Fig. 14(a):

$$\begin{aligned} E &= 2 \times 10^{11} \text{ N/m}^2, & \nu &= 0.3, \\ h_0 &= 1.25 \times 10^9 \text{ N/m}^2, & \sigma_{y0} &= 2.5 \times 10^8 \text{ N/m}^2, \\ \sigma_{ys} &= 2.5 \times 10^8 \text{ N/m}^2, \\ a &= 0, & C &= 0, & \gamma &= 0. \end{aligned}$$

(Case 2) Kinematic hardening material as shown in Fig. 14(c):

$$\begin{aligned} E &= 2 \times 10^{11} \text{ N/m}^2, & \nu &= 0.3, \\ h_0 &= 1.25 \times 10^9 \text{ N/m}^2, & \sigma_{y0} &= 2.5 \times 10^8 \text{ N/m}^2, \\ \sigma_{ys} &= 2.5 \times 10^8 \text{ N/m}^2, \\ a &= 1.0, & C &= 1.0 \times 10^{10} \text{ N/m}^2, & \gamma &= 0. \end{aligned}$$

The axial force–axial displacement curves that correspond to the stress–strain relations in Fig. 14(a) and (c) are shown in Fig. 14(b) and (d), respectively. These numerical results imply that the proper use of a material model is very important to accurately simulate the inelastic buckling behaviors of beam members under cyclic load reversals. It would be a valuable study to investigate the general relations between cyclic stress–strain and axial force–axial displacement curves.

#### 4.3. Cyclic buckling analysis of a square-tube section beam

Considering the square-tube section of TS4  $\times$  4  $\times$  1/2 in Fig. 15(a), we analyze a simply supported beam under cyclic axial displacement, as in the previous section. The beam length is 2.76 m. ASTM-A501 steel and the initial lateral displacement  $\omega = 0.001$  m are used.

Since the coupon test result (that is, the cyclic stress–strain curve) for the material has not been reported [1], we use material properties similar to ASTM-A36 (the same values for  $a$ ,  $C$  and  $\gamma$ ).

(i) For the rapid (initial) yield zone of the first cycle:

$$\begin{aligned} E &= 2 \times 10^{11} \text{ N/m}^2, & \nu &= 0.3, \\ h_0 &= 1.25 \times 10^9 \text{ N/m}^2, & \sigma_{y0} &= 5.3 \times 10^8 \text{ N/m}^2, \\ \sigma_{ys} &= 5.3 \times 10^8 \text{ N/m}^2, \\ a &= 0, & C &= 0, & \gamma &= 0. \end{aligned}$$

(ii) For the smooth hardening zones:

$$\begin{aligned} E &= 2 \times 10^{11} \text{ N/m}^2, & \nu &= 0.3, \\ h_0 &= 1.25 \times 10^9 \text{ N/m}^2, & \sigma_{y0} &= 5.3 \times 10^8 \text{ N/m}^2, \\ \sigma_{ys} &= 5.3 \times 10^8 \text{ N/m}^2, \\ a &= 1.0, & C &= 3.0 \times 10^{10} \text{ N/m}^2, & \gamma &= 300. \end{aligned}$$

In this material, the decreased yield stress after the first yield  $\sigma'_y = 4.3 \times 10^8 \text{ N/m}^2$  is used.

As shown in Fig. 15, the actual section shape of TS4  $\times$  4  $\times$  1/2 is different from the section model used in the numerical analysis. Since the TS4  $\times$  4  $\times$  1/2 plates are comparatively thick and have roundness at the corners of the section, the discrepancy between the actual and model sections is greater than in the W6  $\times$  20 case. Comparing the sectional area and the second moment of area, the section of the proposed numerical model has 10% larger area and 27% larger second moment of area than the actual TS4  $\times$  4  $\times$  1/2 section. To solve this problem, we use the effective section with the shorter lengths of the plate sections shown in Fig. 15(c). The effective section gives a 5.7% smaller area and 1.6% larger second moment of area.

Fig. 16(a) is the experimental response of the axial force–axial displacement relationship when the section in Fig. 15(a) is used. Fig. 16(b) and (c) show the numerical results that correspond

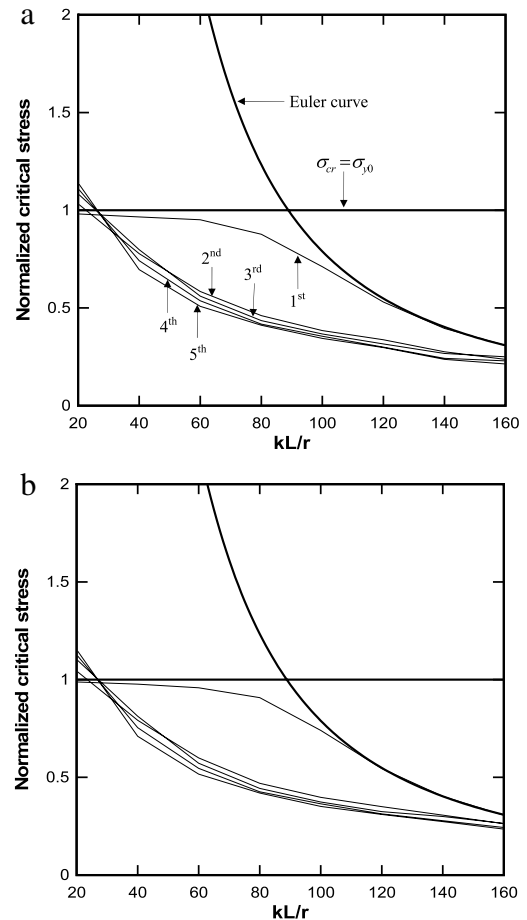


Fig. 21. Normalized critical stress–slenderness ratio curves of W6  $\times$  20 under cyclic load reversals: (a) beam problems with a pinned–pinned boundary; (b) beam problems with a fixed–pinned boundary.

to the sections in Fig. 15(b) and (c), respectively. Note that the numerical result shown in Fig. 16(c) matches the experimental test in Fig. 16(a) well.

We have used the effective section to reduce the difference of sectional properties between the actual section and the section of the numerical model, and the numerical results depending on the sections have been presented. Considering material nonlinearity, it is not easy to model the roundness of the square-tube section. Note that the small difference in sectional shapes can cause a significant change in the response of the cyclic buckling analysis, it is very important to use a proper effective section, as we did in this study.

#### 5. Critical load reduction

In the previous sections, the numerical procedure proposed was verified by comparing the numerical results with the experimental results. Using the numerical procedure, we perform numerical experiments to investigate the phenomenon of critical load reduction under cyclic load reversals depending on the slenderness ratio and initial imperfection. The resulting information can be used to estimate the ultimate load capacity of the failed steel frame structures by buckling and yielding.

It is important to note that, for the critical load reduction, fatigue damage is not considered in this study; however, this effect affects real beam structures subjected to cyclic loading, in particular, when the number of cycles is large.

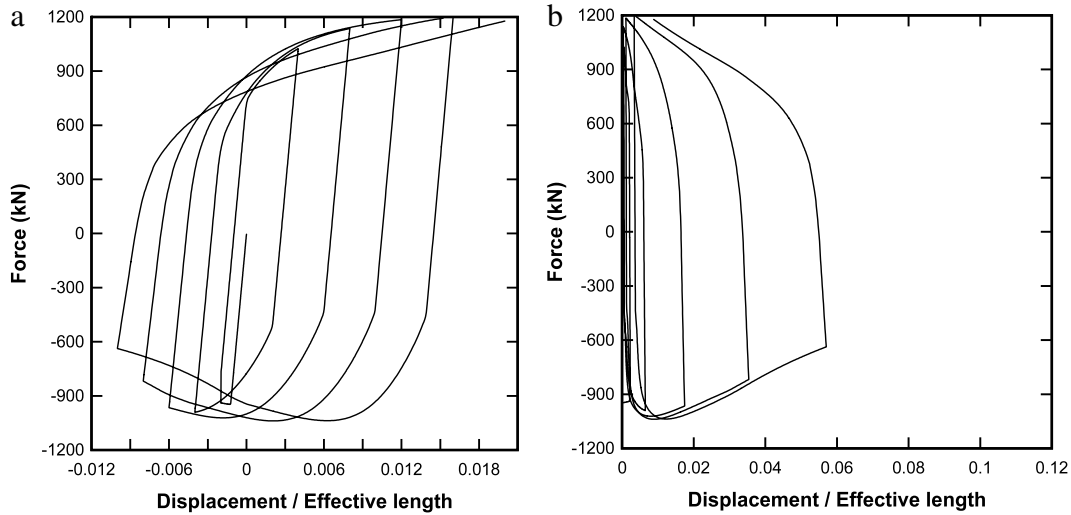


Fig. 22. Load–displacement relations of W6 × 20 for the slenderness ratio of 20: (a) axial force–axial displacement curve; (b) axial force–lateral displacement curve.

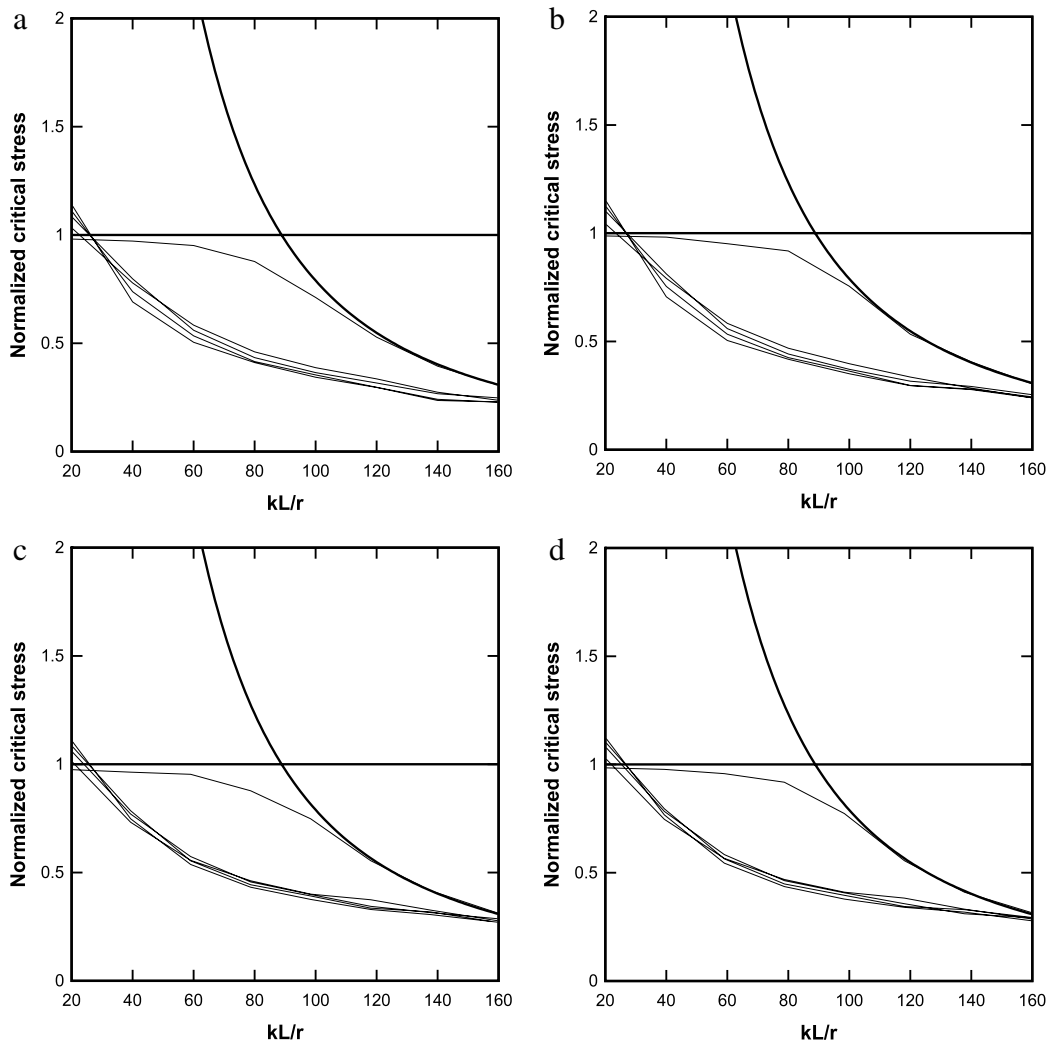


Fig. 23. Normalized critical stress–slenderness ratio curves under cyclic load reversals: (a) pinned–pinned beam problems for W6 × 25; (b) fixed–pinned beam problems for W6 × 25; (c) pinned–pinned beam problems for TS4 × 4 × 1/2; (d) fixed–pinned beam problems for TS4 × 4 × 1/2.

5.1. Effect of the slenderness ratio

For the W6 × 20, W6 × 25 and TS4 × 4 × 1/2 sections, we model a beam problem with pinned ends in Fig. 10(a) and a beam problem

with fixed–pinned conditions at the boundary in Fig. 17(a). By changing the beam length ( $L$ ), slenderness ratios 20, 40, 60, 80, 100, 120, 140 and 160 are considered. The slenderness ratio is given by  $kL/r_g$ ,

$$(15)$$

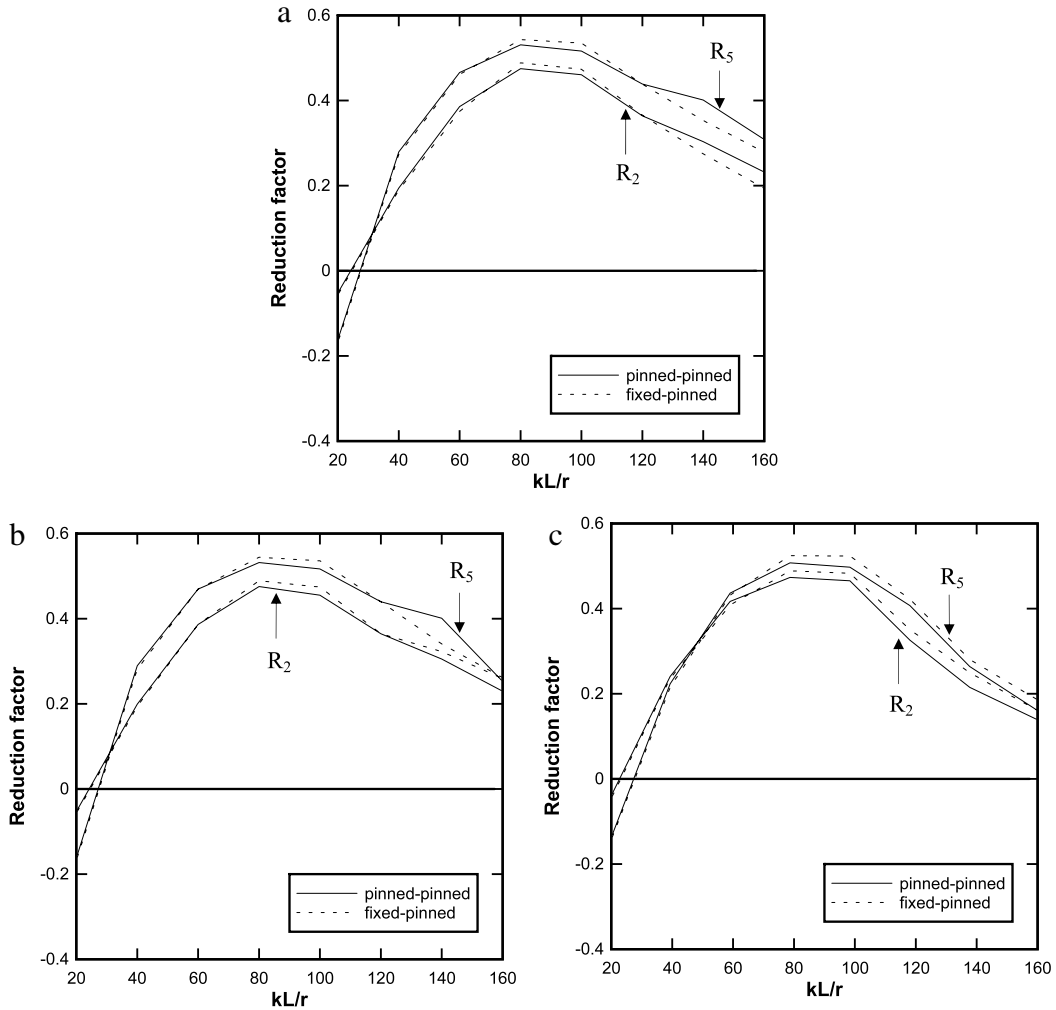


Fig. 24. Critical load reduction factors for (a) W6 × 20, (b) W6 × 25 and (c) TS4 × 4 × 1/2.

where  $k$  is the effective length factor ( $k = 1$  for a pinned–pinned boundary and  $k = 1/\sqrt{2}$  for a fixed–pinned boundary) and  $r_g$  is the radius of gyration,  $\sqrt{I/A}$ .

For all the numerical analyses, we use the same material properties (of ASTM-A36 steel) with mixed hardening as in Section 4.2, and a small imperfection ( $\omega = 0.001$  m) is used at mid-length.

The beam is subjected to the prescribed axial displacement  $\delta$  at the right end. As shown in Fig. 17(b), the prescribed displacement is given by

$$\delta = -\frac{kL}{500} \cdot \frac{N+1}{2} \quad \text{for odd } N \quad \text{and} \quad (16)$$

$$\delta = \frac{kL}{250} \cdot \frac{N}{2} \quad \text{for even } N,$$

where  $N$  denotes the number of half cycles.

For the slenderness ratios 40, 80, 120 and 160, Fig. 18 shows the axial force–axial displacement relationships. As the slenderness ratio increases, we observe that, after the first buckling, sharper peaks appear at subsequent buckling loads and the decreasing buckling load rate becomes smaller. Fig. 19 shows the shape changes of the axial force–lateral displacement curves as a result of different slenderness ratios. Fig. 20 displays the stress distributions in a flange section at mid-length under cyclic load reversals; see Fig. 10(b).

Fig. 21 presents the normalized critical stress under cyclic load reversals

$$\beta = \frac{\sigma_{cr}}{\sigma_{y0}} \quad \text{with } \sigma_{cr} = \frac{P_{cr}}{A}, \quad (17)$$

in which  $P_{cr}$  and  $A$  denote the critical buckling load and sectional area, respectively.

The normalized critical stress that corresponds to the first buckling is enclosed by the Euler curve and the curve corresponding to the yield failure ( $\sigma_{cr} = \sigma_{y0}$ ); see Fig. 21. It is interesting that, when the slenderness ratio is relatively small (that is, for short beams), the consecutive critical loads increase because the effect of the residual lateral displacement is relatively small; see Fig. 22. However, when the beams are not short, the failure of the beams is governed by buckling, and at the second buckling, there is a significant decrease in the critical stresses, and the additional reduction becomes smaller after consecutive bucklings. Note that similar results are obtained for both pinned–pinned and fixed–pinned cases, as shown in Fig. 21(a) and (b).

Fig. 23 shows the normalized critical stress–slenderness ratio curves for the W6 × 25 and TS4 × 4 × 1/2 sections. For all the cases considered, a similar tendency is observed.

Fig. 24 displays the critical load reduction factors depending on the slenderness ratio,

$$R_n = \frac{\sigma_{cr}|_{1st} - \sigma_{cr}|_{nth}}{\sigma_{cr}|_{1st}}. \quad (18)$$

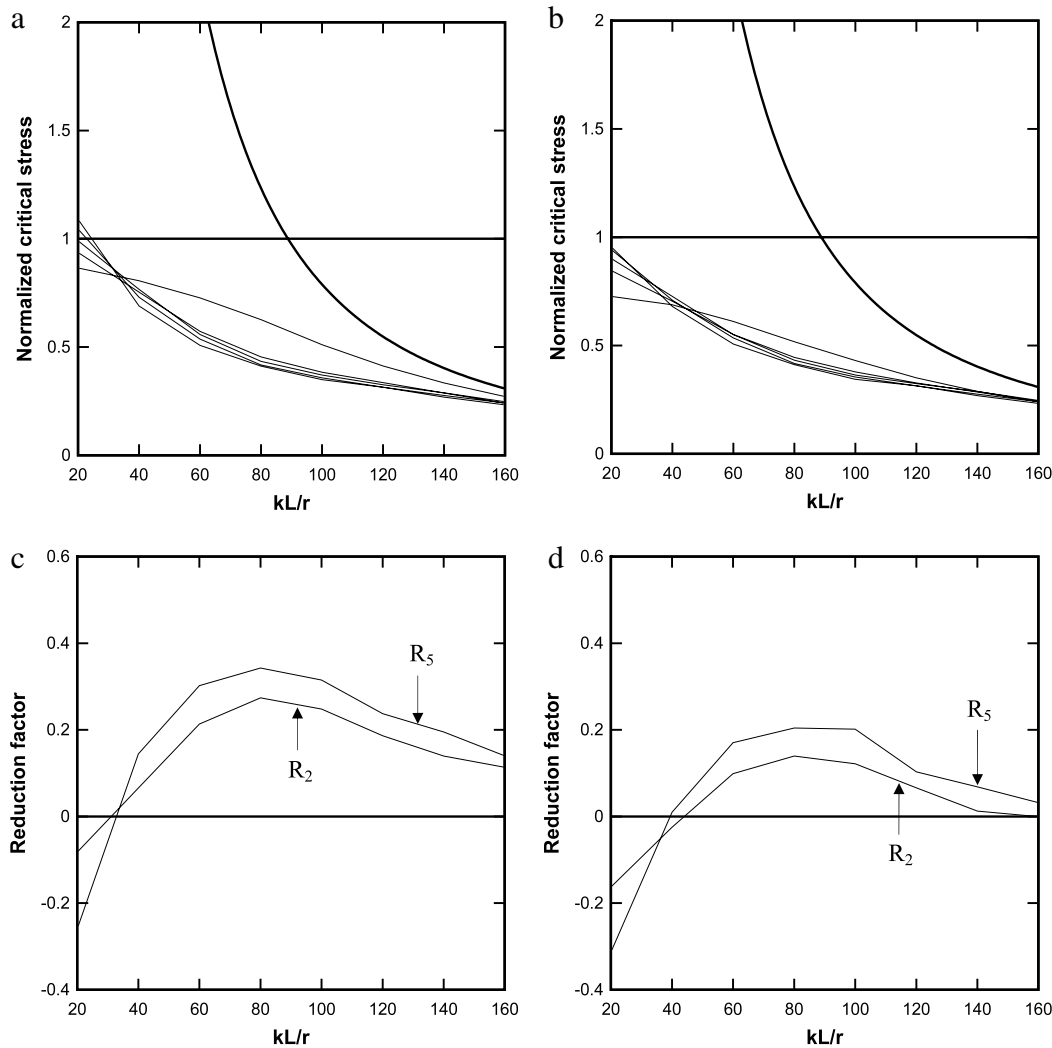


**Fig. 25.** Normalized critical stress–slenderness ratio curves for (a) initial imperfection = 0.01 and (b) initial imperfection = 0.02. Critical load reduction factors for (c) initial imperfection = 0.01 and (d) initial imperfection = 0.02.

In particular, the reduction factor is largest (about 0.5) when the slenderness ratio is 80. Note that the magnitude of the critical load reduction depends on the history of the prescribed displacement, but the trend will be similar.

### 5.2. Effect of initial imperfections

We investigate the effect of initial imperfection on the critical loads under reversed cyclic loading. The beam problem of the  $W6 \times 20$  section with the pinned–pinned condition is considered. Fig. 25 shows the normalized critical stress–slenderness ratio curves and the critical load reduction factor with initial imperfections  $\omega = 0.01$  m and  $\omega = 0.02$  m. Note that the results for initial imperfection 0.001 m are shown in Figs. 21(a) and 24(a).

As the initial imperfection increases, there is a significant decrease in the first buckling load, but the decrease in the consecutive buckling loads is relatively small; see Figs. 21(a), 25(a) and (b). In particular, for long beams, the decreases in both the first and consecutive buckling loads are smaller than for short and intermediate beams. As a result, the reduction factor decreases as the initial imperfection increases; see Figs. 24(a), 25(c) and (d).

It is well known that hot-rolled beams are not uniformly cooled in production, and the resulting residual stress has an effect on the critical load under buckling as an initial imperfection [17]. Using the numerical model proposed in this study, the effect of the residual stress would be simulated as in [5].

## 6. Conclusions

In this study, to simulate the inelastic buckling behavior of beams with various structural thin-walled sections and a proper material model with the cyclic stress–strain relation. To show the validity of the numerical procedure proposed, a two-node beam finite element is implemented in an analysis code. We then numerically simulated the inelastic cyclic buckling of wide-flange and square-tube section beams, and the results were compared with those of the experimental tests. The finite element procedure, including the material model, simulated a good estimate of the inelastic buckling behavior of beam members under reversed cyclic loadings. Finally, we performed numerical experiments to investigate the reduction behavior of the critical load under cyclic load reversals depending on the slenderness ratio and initial imperfection, and the results have been discussed in detail.

Through the inelastic buckling analyses of steel members under reversed cyclic loading, we have made the following observations.

- To correctly predict the inelastic hysteresis behavior of steel beams, it is very important to use a material model that can properly simulate the cyclic stress–strain behavior of steel.
- The problem of discrepancies between numerical models and actual sections can be overcome by using the effective section concept, which gives results with better accuracy.

- The critical load reduction factor is largest when the slenderness ratio is around 80. For long beams, the reduction factor is small, and the buckling loads increase slightly for short beams.
- After the first buckling, the normalized critical stress–slenderness ratio curves do not depend greatly on initial imperfections, especially when the slenderness ratio is larger.

In this study, we did not consider lateral buckling, fatigue damage, residual stress by production and other effects and behaviors. Such considerations remain for future studies.

## References

- [1] Black RG, Wenger WA, Popov EP. Inelastic buckling of steel struts under cyclic load reversal. Report No: EERC-80/40. Earthquake Engineering Research Center. Berkeley (CA): University of California; 1980.
- [2] Ikeda K, Mahin SA, Dermitzakis SN. Phenomenological modeling of steel braces under cyclic loading. Report No: EERC-84/09. Earthquake Engineering Research Center. Berkeley (CA): University of California; 1984.
- [3] Mahin SA, Uriz P. Seismic performance assessment of special concentrically braced steel frames. In: Proc of international workshop on steel and concrete composite constructions. Taiwan: National Center for Research on Earthquake Engineering (NCREE); 2003. p. 1–15.
- [4] Han DJ, Chen WF. Buckling and cyclic inelastic analysis of steel tubular beam–columns. *Eng Struct* 1983;5:119–32.
- [5] Mamaghani IHP, Usami T, Mizuno E. Inelastic large deflection analysis of structural steel members under cyclic loading. *Eng Struct* 1996;18:659–68.
- [6] Maison BF, Popov EP. Cyclic response prediction for braced steel frames. *J Struct Eng, ASCE* 1980;106(7):1401–16.
- [7] Dicleli M, Mehta A. Simulation of inelastic cyclic buckling behavior of steel box sections. *Comput Struct* 2007;85:446–57.
- [8] Dicleli M, Calik EE. Physical theory hysteretic model for steel braces. *J Struct Eng, ASCE* 2008;134(7):1215–28.
- [9] Krishnan S, Hall JF. Modeling steel frame building in three dimensions. II: elastofiber beam element and examples. *J Eng Mech* 2006;132:359–74.
- [10] Bathe KJ. Finite element procedures. New York: Prentice Hall; 1996.
- [11] Lee PS, McClure G. A general 3D L-section beam finite element for elastoplastic large deformation analysis. *Comput Struct* 2006;84:215–29.
- [12] Lee PS, McClure G. Elastoplastic large deformation analysis of a lattice steel tower structure and comparison with full-scale tests. *J Constr Steel Res* 2007;63:709–17.
- [13] Kojić M, Bathe KJ. Inelastic analysis of solids and structures. New York: Springer; 2005.
- [14] Anand L. Constitutive equations for hot-working of metals. *Int J Plast* 1985;1:213–31.
- [15] Brown SB, Kim KH, Anand L. An internal variable constitutive model for hot working of metals. *Int J Plast* 1989;5:95–130.
- [16] White CS, Bronkhorst CA, Anand L. An improved isotropic–kinematic hardening model for moderate deformation metal plasticity. *Mech Mater* 1990;10:127–47.
- [17] Bažant ZP, Cedolin L. Stability of structures. New York: Oxford University Press; 1991.